Identifying the limits of strain engineering in $NaNbO_3$ ultrathin films

Shengwei Zeng[1,], Khuong Phuong Ong[2], Samantha Faye Duran Solco[1], Zhi Shiuh Lim[1], Qibin Zeng[1], Baichen Lin[1,3], Jiangbo Luo[4], Wenting Zhao[3], Tiancheng Luo[1], Weifan Cai[1], Zhen Ye[1,5], Celine Sim[1,3], Chee Kiang Ivan Tan[1], Seeram Ramakrishna[5], Yeng Ming Lam[3,6], A. Ariando[4], Huajun Liu[1,3,*]*

[1]Institute of Materials Research and Engineering (IMRE), Agency for Science, Technology and Research (A*STAR), 2 Fusionopolis Way, Innovis #08-03, Singapore 138634, Republic of Singapore

[2]Institute of High Performance Computing (IHPC), Agency for Science, Technology and Research (A*STAR), Singapore 138632, Republic of Singapore

[3]School of Materials Science and Engineering, Nanyang Technological University, 50 Nanyang Avenue, Singapore 639798, Republic of Singapore

[4]Department of Physics, Faculty of Science, National University of Singapore, Singapore 117551, Republic of Singapore

[5]Department of Mechanical Engineering, National University of Singapore, 9 Engineering Drive 1, Singapore 117575, Republic of Singapore

[6]Facility for Analysis, Characterisation, Testing and Simulation (FACTS), Nanyang Technological University, Singapore 639798, Republic of Singapore

E-mail: liu_huajun@imre.a-star.edu.sg; zeng_shengwei@imre.a-star.edu.sg

KEYWORDS: strain engineering, $NaNbO_3$, ferroelectrics, thin films, functional oxides

ABSTRACT: Epitaxial $NaNbO_3$ ultrathin films are grown on single crystal substrates with a wide range of compressive (-6.24%) and tensile (+7.13%) strain. High-resolution X-ray diffraction reveals a coherently strained state of $NaNbO_3$ thin films within the strain range from -1.42 % to 1.86 %, beyond which the films are in relaxed states. This is accompanied by a change in the growth mode from step-flow growth in strained films to coalesced island growth in relaxed films. Piezoresponse force microscopy measurements, including domain writing and reading, reveal a single vertical ferroelectric domain for the compressive films, while the tensile films exhibit a mixture of multiple vertical domains. The first-principles calculations confirm the stability of the strained $NaNbO_3$. Our results provide important information for the understanding and engineering of strained functional thin films.

INTRODUCTION

Ferroelectric and piezoelectric materials have shown promising device applications in various aspects such as memory, actuators, transducers, sensors, and radio-frequency devices [1, 2]. As the ferroelectric orders are determined by the crystal structure, structural modification which could be realized by strain engineering have been shown to be a practical approach towards tailoring of physical properties [3]. More importantly, ferroelectrics in the form of thin films on suitable substrates with appropriate strain exhibited properties that are greatly superior to their bulk counterparts, enabling the realization of device applications with high performance [4, 5]. For examples, significant enhancements in ferroelectricity have been demonstrated in strained perovskite $BaTiO_3$, $SrTiO_3$, $BiFeO_3$ and $PbTiO_3$ thin films [6-9]. Moreover, strain engineering on perovskite oxide also modifies the charge, spin, orbital, and lattice degrees of freedom, thereby allowing for great flexibility in tailoring new and versatile functionalities in ferroelectrics. Thus, a comprehensive understanding of the effect of epitaxial strain on deposition, structure and ferroelectric phase is critical for precise property tuning.

$NaNbO_3$ (NNO), a typical compound of alkaline niobate-based materials, exhibit promising electromechanical and dielectric properties which make them interesting for (anti-)ferroelectric and piezoelectric applications [10-15]. Especially the orthorhombic antiferroelectric phase (space group *Pbma*) can be stable across a wide temperature range (359°C to -100°C), therefore, NNO has recently gained attention in a range of practical applications, including electrostatic energy storage capacitors, thermal switches and multi-state memory devices [13, 16-20]. Additionally, NNO exhibits rich crystalline phases under various external stimuli, making it an ideal candidate for studying the effects of strain [13, 14, 17]. However, the preparation of high-quality NNO thin films is challenging due to the volatilization of Na elements during the deposition process [21]. Recently, NNO thin films have been grown by metal-organic chemical

vapor deposition technique and the strain-induced structural phase transition [22, 23], an enhancement of in-plane permittivity and tunability have been observed [24]. NNO films grown by pulsed laser deposition technique showed a strain effect on the antiferroelectricity [25, 26]. Additionally, size effect-induced ferroelectricity in antiferroelectric film has been observed in the free-standing NNO thin films [27]. However, the extent of strain state in previous studies, induced by lattice mismatch between NNO thin films and substrates are only limited on the substrates with comparable lattice constant of NNO. To comprehensively investigate the strain effect on NNO, lattice mismatch with a wide range is desirable. This could be realized through the preparation of high-quality ultrathin film and usage of substrates with a wide range of in-plane lattice constants as compared to that of bulk NNO.

In this paper, we comprehensively investigate the strain effect on the growth modes, crystal structures, ferroelectric domains of 20-nm-thick NNO thin films on various substrates with a wide range of in-plane lattice constants. The film thickness of approximately 20 nm was chosen to prevent thickness induced strain relaxation, while also providing a sufficient thickness for structural characterization by X-ray diffraction reciprocal space mapping. The lattice mismatch between NNO and substrates are varied in a wide range from -6.24 % (compressive strain) to 7.13% (tensile strain). The first-principles calculations are also performed to investigate the energy versus strain state relationship and suggest an energy range for fully strained NNO thin films.

EXPERIMENTAL SECTION AND THEORETICAL CALCULATIONS

Sample preparation and characterization: The ceramic target with 5% sodium (Na) excess and the nominal composition of $Na_{1.05}NbO_3$ was prepared by conventional solid-state reaction using Na_2CO_3 and Nb_2O_5 powder as the raw materials. The purpose of using excess Na is to

compensate the Na loss that occurs during the growth process at high temperature. The NNO thin films with thickness of approximately 20 nm were grown on different single-crystal substrates using a pulsed laser deposition (PLD) technique with a 248-nm KrF excimer laser ablation on the ceramic target surface. The substrates include (001)-oriented MgO (abbreviated as 001, MgO), $(PbMg_{0.33}Nb_{0.67})_{1-x}$:$(PbTiO_3)_x$ (x=0.29-0.32, 001, PMNPT), $KTaO_3$ (001, KTO), $GdScO_3$ (110, GSO), $DyScO_3$ (110, DSO), $SrTiO_3$ (001, STO), $NdGaO_3$ (110, NGO), $LaAlO_3$ (001, LAO), $SrLaAlO_4$ (001, SLAO), $NdCaAlO_3$ (001, NCAO). The deposition temperature and oxygen partial pressure P_{O2} for NNO thin films were 600 ºC and 150 mTorr, respectively. The laser energy density on the target surface was set to 1.2 Jcm^{-2}, and the pulse repetition frequency was 10 Hz. After deposition, the samples were cooled down to room temperature at a rate of 8 ºC/min and at P_{O2} = 300 Torr. The film morphology and ferroelectric domain structures were measured using a piezoresponse force microscopy (PFM, Bruker) with a Pt coated probe (OPUS 240AC-PP). The amplitude and phase images represent the strength of the piezoresponse and the polarization orientation respectively. The crystal structure characterization was performed by high-resolution X-ray diffraction (XRD) and low-angle X-ray reflectivity (XRR) (Smartlab, Rigaku) with an X-ray wavelength of λ = 1.5405 Å.

First-principles calculations: The crystal structures of $NaNbO_3$ within different symmetry of *P4mm* and *Pm* are studied using the first principles calculations within GGA-PBESol approximation [28], as implemented in the WIEN2K software package, the fully localized limit using full-potential (linearized) augmented planewave (FP-LAPW) + local orbital method [29]. The simulations have been calculated with the augmented plane wave + local orbital (APW+ lo) basis set and the muffin-tin radii (R_{MT}) for the atomic spheres were chosen as: 2.12 a.u, 1.78 a.u, and 1.61 a.u for Na, Nb, O, respectively. The partial waves were expanded up to l_{max} =10 in the muffin-tin spheres and outside a planewave cutoff K_{max} defined by $R_{min}K_{max}$ =8.0 was used. The charge density was Fourier-expanded up to $R_{min}G_{max}$ =20.0. Here, R_{min} is the

minimum sphere radius, i.e., 1.61 a.u. The Na $2s^2 2p^6 3s^1$, Nb $4s^2 4p^6 4d^4 5s^1$, and O $2s^2 2p^4$ were treated as semi-core states, and were included in the valence. The Brillouin zone sampling was done using a Kmesh of 10×10×10 k-points in the full Brilluoin zone for P4mm and Pm structures. All structures are fully relaxed by using energy minimization with Hellmann-Feynman force of 1 mRy/a.u. The in-plane strain is defined as $\eta = (a - a_0)/a_0$, where a_0 is the in-plane lattice constant of the most stable structure (a_0 = 3.92 Å in our case which is obtained from ab initio optimization for *P4mm* structure). For each strain state, i.e., different in-plane lattice constant *a*, lattice constant *c* and all atomic positions were fully relaxed until the final Hellmann-Feynman forces were less than 1 mRy/a.u. For the Pm symmetry, our study, see **Figure S1-S2**, show that Pm structures is stable with angle b=89.8°.

RESULTS AND DISCUSSION

The realization of compressive and tensile strain in the epitaxial NNO films are achieved due to the in-plane lattice parameter mismatches between the films and substrates. The bulk lattice parameters of NNO shown here are based on pseudocubic notation: $a_{pc} = b_{pc}$ = 3.915 Å, c_{pc} = 3.88 Å, calculated from orthorhombic lattice parameters of bulk NNO in the antiferroelectric ground state (orthorhombic, *Pbma*, a_o = 5.566 Å, b_o = 15.52 Å, c_o = 5.506 Å) [30, 31], as shown in **Figure 1(a)**. The in-plane lattice parameters of substrates range from 4.21 to 3.685 Å and the in-plane lattice mismatch between NNO and substrates are shown in **Figure 1(b)** [32]. The lattice mismatch is calculated using the formula $\Delta a/a = (a_s - a_b)/a_s$, where a_s is the lattice parameter of the substrate and a_b is the lattice parameter NNO bulk, respectively. To simplify the demonstration, we calculate the lattice mismatch assuming that the NNO thin films are oriented along $(001)_{pc}$ orientation on the substrates. One can see that both tensile and

compressive strain can be induced in NNO by the substrates, with the lattice mismatch tunable from -6.24 % (compressive) to 7.13 % (tensile).

Figure 1(c) shows the low-angle X-ray reflectivity (XRR) of approximately 20 nm NNO thin films on various substrates. Clear reflectance oscillations indicate high quality of thin films as well as smooth surfaces and interfaces, except for the film on MgO substrate. The absence of reflectance oscillations in NNO on MgO can be attributed to the rough surface caused by the large lattice mismatch. **Figure 1(d)** shows the X-ray Diffraction (XRD) θ-2θ scans of NNO thin films within the 2θ angles range from 20 to 26°. The clear (001) Bragg diffraction peaks and finite-thickness oscillations further indicate high crystal quality of NNO thin films. The θ-2θ scans in a wide-angle range from 20 to 110° are shown in **Figure S3**. Only the (00*l*) perovskite peaks are observed, where *l* is an integer, confirming the single-orientation epitaxial growth and the absence of secondary phase of NNO films. For the films with compressive strain (negative $\Delta a/a$), the out-of-plane lattice constant *c*, calculated from the XRD θ-2θ scans, increases with increasing lattice mismatch, and reaches a maximum of 3.952 Å at $\Delta a/a$ = -1.42 % at the negative side (*i.e.*, NGO substrate). This indicates that NNO undergoes an increasingly compressive strain (**Figure 1(e)**). As the $\Delta a/a$ is smaller than -1.42 % at the negative side, the *c* starts to decrease, suggesting that NNO is relaxed due to the large lattice mismatch. For the films with tensile strain (positive $\Delta a/a$), the *c* decreases with increasing $\Delta a/a$ and reaches a minimum of 3.855 Å at $\Delta a/a$ = 1.86 % (*i.e.*, KTO substrate), then increases with further increasing $\Delta a/a$ up to 7.13 %. The increase in *c* at tensile lattice mismatch higher than 1.86% could also be attributed to the relaxation of NNO.

The *c*, in-plane lattice constants *a* which is calculated from reciprocal space maps (RSMs) as shown in the following text, *c*/*a* ratio and unit cell volume *versus* lattice mismatch are summarized as a phase diagram in **Figure 1(e) and 1(f)**. The phase diagram can be separated

into the relaxed ($\Delta a/a$ < -1.42%), fully strained (-1.42 % < $\Delta a/a$ < 1.86 %) and relaxed ($\Delta a/a$ > 1.86 %) regions. In the fully strained region, *a* and the unit cell volume decrease, while *c* and *c*/*a* ratio increase monotonously as the lattice mismatch decreases, indicating that NNO undergoes an increasingly compressive strain. Conversely, in both the relaxed regions, they show opposite trends as the absolute values of lattice mismatch increases. With the measured in-plane lattice constants of NNO thin films, we could calculate the in-plane lattice mismatch between NNO bulk and the deposited NNO thin films, using the formula $(\Delta a/a)_{NNO} = (a_f - a_b)/a_f$, where a_f is the in-plane lattice parameter of the NNO films and a_b is the lattice parameter NNO bulk, respectively. As shown in **Figure 1(b)**, $(\Delta a/a)_{NNO}$ linearly increases with the in-plane lattice constants of substrate in the strained region, while it is close to bulk values in the relaxed regions.

To further characterize the strain state of NNO thin films, we performed the RSM measurements, as shown in **Figure 2**. No diffraction spot splitting is observed in either the Q_x direction (characterizing the in-plane lattice structure) or Q_z direction (characterizing the out-of-plane lattice structure) for NNO thin films. This indicates the absence of phase separation in the NNO films deposited on various substrates, even across a wide range of lattice mismatch. For the thin films under tensile strain, they are fully strained as $\Delta a/a$ increases up to 1.86 % (on KTO substrate), as evidenced by the identical in-plane scattering vector components (i.e., Q_x values) of the films and substrates. Additionally, the constrained (-103) reflection spots and clear Laue oscillations in the vicinity of the (001) peak (**Figure 1(d)**) are observed, indicating that the high sample quality is maintained even under large tensile strain. As lattice mismatch exceeds 1.86 % (on PMNPT and MgO substrates), the films become relaxed, as evidenced by the deviation of the Q_x values of the films away from those of the substrates in the RSMs. A similar trend is observed for thin films grown on substrates with compressive strain: the films are fully strained for $\Delta a/a$ up to -1.42 % (on NGO substrate) but become relaxed as $\Delta a/a$

increases further. Within the fully strained region, the in-plane lattice constants of NNO thin films, *a*, increase with in-plane lattice constants of the substrates. Conversely, in the relaxation regions, the lattice constants show an opposite trend in both tensile and compressive directions (**Figure 1(e)**). Therefore, the strain states of NNO thin films exhibit a generally symmetric behaviour with respect to lattice mismatch, whether under tensile or compressive strain.

The *c*/*a* ratio of NNO thin films exhibits mainly linear behaviour in relation to lattice mismatch within the fully strained region (**Figure 1(f)**), indicating that the tetragonal deformation of the films is dominated by biaxial strain. In the fully strained region, we plot the out-of-plane lattice strain ε_{zz} against the in-plane lattice strain ε_{xx} for NNO thin films, as shown in **Figure 3**. Using the ε_{zz} *versus* ε_{xx} relationship, we can calculate the Poisson's ratio, an important mechanical parameter that characterizes deformation of a material in the direction perpendicular to the applied strain. For the thin film subjected to biaxial stress, the Poisson's ratio (v) can be calculated using the formula $v = 1/(1-2\varepsilon_{xx}/\varepsilon_{zz})$ [33, 34]. The $\varepsilon_{zz}/\varepsilon_{xx}$ value for NNO thin films is estimated through linear fitting of the ε_{zz} *versus* ε_{xx} data (**Figure 3**), which gives a Poisson's ratio of $v = 0.28$. The obtained Poisson's ratio for NNO thin film is comparable to the typical values of most oxide materials [33-37].

To investigate the strain effects on the ferroelectric domain structures, we performed the piezoresponse force microscopy (PFM) measurements on the NNO thin films grown on various substrates [38], as shown in **Figure 4**. The corresponding atomic force microscopy (AFM) and vertical PFM amplitude images are shown in **Figure S4 and Figure S5**. The surface morphology and growth mode of NNO films show an obvious evolution with varying lattice mismatch. The films with lower $\Delta a/a$ show a low root-mean-square (RMS) roughness of less than 0.32 nm (**Figs. S4(c)-S4(h)**). Especially, the surface of fully strained NNO films on GSO, DSO, STO, and NGO show a step-and-terrace structure (**Figs. S4(d)-S4(g)**), indicating a two-

dimensional step-flow growth on the substrates with low lattice mismatch. In contrast, NNO depositions on substrates with larger $\Delta a/a$ exhibit coalesced three-dimensional islands on the surfaces and the RMS roughness larger than 0.74 nm (**Figs. S4a), S4(b), S4(i) and S4(j)**). This is because, for the substrates with a large lattice mismatch, the initial layer of the film experiences significant stress, which causes the ablated species arriving on the surface to exhibit reduced kinetic energy. As a result, fewer adatoms are able to overcome the diffusion barrier, leading to the formation of islands [39]. Therefore, for the NNO deposition by the PLD technique, a two-dimensional growth mode is favoured for the films under low strain conditions, whereas a three-dimensional island growth mode is more favourable for the films with either high compressive or tensile lattice strain. A similar change in surface morphology with strain could be seen on the films grown by metal–organic chemical vapour deposition (MOCVD) [22]. The change in growth mode of NNO thin films has also been reported through variations in deposition parameters, such as oxygen partial pressure [35].

With respect to the ferroelectric domains, we observe clear contrast (dark and bright) in the vertical phase images of NNO films with tensile strain (on MgO, PMN-PT, KTO, GSO and DSO) and near the bulk state (on STO), indicating the presence of multidomain with vertical polarization direction pointing down and up, respectively (**Figure 4(a)- 4(f)**). It should be noted that vertical domains are still present even in highly tensile films. This may be due to the symmetry constraints in NNO imposed by substrate strain, which only allows the displacement of niobium atoms within oxygen octahedra along the out-of-plane direction. For the films with compressive strain (on NGO, LAO, SLAO, and NCAO), the polarization directions tend to align in a single direction, as indicated by the negligible vertical phase contrast (**Figure 4(g)-4(j)**). These indicate that compressive strain favors the formation of single vertical domains, while tensile strain and bulk-like NNO promote multiple vertical domains. Similar single vertical domains have been also observed in ultrathin $BiFeO_3$ and $BaTiO_3$ thin films with

compressive strain [40, 41]. In addition, 20-nm NNO thin films with a 15-nm $La_{0.67}Sr_{0.33}MnO_3$ thin film as bottom electrode were prepared, and PFM was utilized to write and read domain patterns. As shown in **Figure S6**, domain pattern writing and reading were achieved through voltage poling, resulting in a ~180° phase difference in the PFM image, clearly confirming the formation of ferroelectric domains in the NNO thin films. One might assume that strain in thin films changes gradually as the film thickness increases, leading to a gradual transition in the internal domain structure. However, considering the ultrathin nature of the NNO films, the small full width at half maximum of the XRD rocking curve (**Figure S7**), and the smooth surface (**Figure S4**), the films demonstrate high quality and homogeneity. This indicates that the observed domain structures are uniform throughout the thin film.

It has been reported that tensile-strained NNO thin films deposited on $DyScO_3$ (110) substrates exhibit regular nanometer-sized stripe domains [35, 42]. In the ultrathin NNO films presented in these reports, the domains form a priodic a1/a2/a1/a2 stripe pattern along the [001] direction of DSO substrate, attributed to octahedral coupling across the substrate/film interface [43]. In thicker films, the domain configuration evolves into a coexistence of a_1/a_2 (in-plane polarization) and *c*-domains (out-of-plane polarization), which is associated with the gradual relaxation of tensile strain as the film thickness increases [35, 42, 44]. However, such stripe domains are absent in our NNO thin films on the same DSO substrate. The formation of ferroelectric domain in thin films is determined not only by lattice strain but also by the elemental composition and structural/compositional ordering [45-48]. Therefore, the difference in domain patterns of NNO may stem from variations in structural and/or compositional disorder between our samples and those in previous reports. Indeed, in reference [35, 42], the ceramic target used for thin film deposition had a Na/Nb ratio of 1.17, which is much higher than the ratio of 1.05 in the target used in our current study, potentially leading to Na excess and the stripe domains in NNO films of previous reports [35, 42].

To better understand the strain effect on the lattice structure of epitaxial NNO thin films, we performed the first-principles calculations. As the XRD data showed absence of phase separation, the epitaxial films on various substrates possess the tetragonal structure. The calculated energy *versus* in-plane lattice mismatch curve for tetragonal NNO (space group *P4mm*) is shown in **Figure 5(a)**. One can see that the fully strained region is consistent with the region exhibiting lower energy below 70 meV/f.u., as shown in dashed black rectangle. The energy curve of NNO with monoclinic structure (space group *Pm*) is also calculated and shows a similar energy range for the strained region. Similar energy curves and energy ranges in the fully strained region are observed even if the NNO structure is modified, indicating the robust relationship between the energy and epitaxial strain. **Figure 5(b)** summarizes the schematic ferroelectric domain structures for NNO thin films based on the PFM measurements. Single vertical domain is observed in compressive NNO thin films, while multiple vertical domains are observed in tensile and bulk-like films. This paves an avenue for domain engineering in NNO thin films.

CONCLUSIONS

In summary, ultrathin NNO films deposited on different substrates exhibit a fully strained state within small lattice mismatch region between -1.42 % and 1.86 %, while it is relaxed as both the compressive and tensile lattice mismatch increases beyond the critical values. The growth mode of NNO changes from a two-dimensional step-flow growth to a three-dimensional coalesced island growth as the lattice mismatch increases. The relationship between out-of-plane lattice strain and in-plane lattice strain for NNO thin films in the fully strained region gives a Poisson's ratio of $\nu = 0.28$ for NNO. The first-principles calculations suggest an energy limit (below 70 meV/f.u.) to stabilize the strained NNO, beyond which the films are relaxed.

The ferroelectric domain structures also exhibit a strain dependence, with compressive films displaying a single vertical domain, while tensile and bulk-like films show multiple vertical domains. These findings establish a powerful framework for leveraging strain to engineer the structural and functional properties of ferro- and piezoelectric oxide thin films, unlocking new possibilities for advanced material design.

ASSOCIATED CONTENT

Supporting Information

The Supporting Information is available free of charge at https://pubs.acs.org. The calculated total energy *versus* in-plane lattice constant (Figure S1); The total energy *versus* c-lattice constant (Figure S2); Structure parameters for first-principles calculations (Table S1). XRD in a wide 2θ angle range between 20-110^{o} (Figure S3); AFM images (Figure S4); The vertical PFM amplitude images (Figure S5); PFM domain writing and reading (Figure S6); XRD rocking curve (Figure S7).

AUTHOR INFORMATION

Corresponding Authors

Shengwei Zeng - Institute of Materials Research and Engineering (IMRE), Agency for Science, Technology and Research (A*STAR), 2 Fusionopolis Way, Innovis #08-03, Singapore 138634, Republic of Singapore; Email: zeng_shengwei@imre.a-star.edu.sg

Huajun Liu - Institute of Materials Research and Engineering (IMRE), Agency for Science, Technology and Research (A*STAR), 2 Fusionopolis Way, Innovis #08-03, Singapore 138634, Republic of Singapore; Email: liu_huajun@imre.a-star.edu.sg

Authors

Khuong Phuong Ong - Institute of High Performance Computing (IHPC), Agency for Science, Technology and Research (A*STAR), Singapore 138632, Republic of Singapore

Samantha Faye Duran Solco - Institute of Materials Research and Engineering (IMRE), Agency for Science, Technology and Research (A*STAR), 2 Fusionopolis Way, Innovis #08-03, Singapore 138634, Republic of Singapore

Zhi Shiuh Lim - Institute of Materials Research and Engineering (IMRE), Agency for Science, Technology and Research (A*STAR), 2 Fusionopolis Way, Innovis #08-03, Singapore 138634, Republic of Singapore

Qibin Zeng - Institute of Materials Research and Engineering (IMRE), Agency for Science, Technology and Research (A*STAR), 2 Fusionopolis Way, Innovis #08-03, Singapore 138634, Republic of Singapore

Baichen Lin - Institute of Materials Research and Engineering (IMRE), Agency for Science, Technology and Research (A*STAR), 2 Fusionopolis Way, Innovis #08-03, Singapore 138634, Republic of Singapore; School of Materials Science and Engineering, Nanyang Technological University, 50 Nanyang Avenue, Singapore 639798, Republic of Singapore

Jiangbo Luo - Department of Physics, Faculty of Science, National University of Singapore, Singapore 117551, Republic of Singapore

Wenting Zhao - School of Materials Science and Engineering, Nanyang Technological University, 50 Nanyang Avenue, Singapore 639798, Republic of Singapore

Tiancheng Luo - Institute of Materials Research and Engineering (IMRE), Agency for Science, Technology and Research (A*STAR), 2 Fusionopolis Way, Innovis #08-03, Singapore 138634, Republic of Singapore

Weifan Cai - Institute of Materials Research and Engineering (IMRE), Agency for Science, Technology and Research (A*STAR), 2 Fusionopolis Way, Innovis #08-03, Singapore 138634, Republic of Singapore

Zhen Ye - Institute of Materials Research and Engineering (IMRE), Agency for Science, Technology and Research (A*STAR), 2 Fusionopolis Way, Innovis #08-03, Singapore 138634, Republic of Singapore; Department of Mechanical Engineering, National University of Singapore, 9 Engineering Drive 1, Singapore 117575, Republic of Singapore

Celine Sim - Institute of Materials Research and Engineering (IMRE), Agency for Science, Technology and Research (A*STAR), 2 Fusionopolis Way, Innovis #08-03, Singapore 138634, Republic of Singapore; School of Materials Science and Engineering, Nanyang Technological University, 50 Nanyang Avenue, Singapore 639798, Republic of Singapore

Chee Kiang Ivan Tan - Institute of Materials Research and Engineering (IMRE), Agency for Science, Technology and Research (A*STAR), 2 Fusionopolis Way, Innovis #08-03, Singapore 138634, Republic of Singapore

Seeram Ramakrishna - Department of Mechanical Engineering, National University of Singapore, 9 Engineering Drive 1, Singapore 117575, Republic of Singapore

Yeng Ming Lam - School of Materials Science and Engineering, Nanyang Technological University, 50 Nanyang Avenue, Singapore 639798, Republic of Singapore; Facility for Analysis, Characterisation, Testing and Simulation (FACTS), Nanyang Technological University, Singapore 639798, Republic of Singapore

A. Ariando - Department of Physics, Faculty of Science, National University of Singapore, Singapore 117551, Republic of Singapore

ACKNOWLEDGEMENTS

The authors acknowledge the funding support by RIE2025 MTC Individual Research Grant (M22K2c0084), National Research Foundation Competitive Research Program (NRF-CRP28-2022-0002), Career Development Fund (C210812020) and Central Research Fund, A*STAR, Singapore. L.J. and A.A. acknowledges support by Ministry of Education (MOE), Singapore, under its Tier-2 Academic Research Fund (AcRF), grant no.MOE-T2EP50121-0018 and MOE-T2EP50123-0013, by the MOE Tier-3 Grant (MOE-MOET32023-0003) 'Quantum Geometric Advantage' and by the SUSTech-NUS Joint Research Program.

Author contributions

S.Z. and H.L. conceived the idea and designed the experiments; K.P.O. performed the first-principles calculations; S.Z., Z.S.L. and J.L. grew the thin films; S.F.D.S., S.Z., B.L., Z.Y. and C.S. carried out the XRD characterization; S.Z., W.Z., Q.Z., T.L. and W.C. carried out AFM and PFM measurements; S.Z., H.L., K.P.O., C.K.I.T., S.R., Y.M.L. and A.A. wrote and revised

the paper with inputs from others. All authors contributed to the data analysis and manuscript revisions.

Notes

The authors declare no conflict of interest.

REFERENCES

[1] G. H. Haertling, Ferroelectric ceramics: history and technology, *Journal of the American Ceramic Society*, **82**, 797 (1999).

[2] N. Setter, D. Damjanovic, L. Eng, G. Fox, S. Gevorgian, S. Hong, A. Kingon, H. Kohlstedt, N. Park, G. Stephenson, I. Stolitchnov, A. K. Taganstev, D. V. Taylor, T. Yamada, and S. Streiffer, Ferroelectric thin films: Review of materials, properties, and applications, *Journal of Applied Physics*, **100**, 051606 (2006).

[3] A. R. Damodaran, J. C. Agar, S. Pandya, Z. Chen, L. Dedon, R. Xu, B. Apgar, S. Saremi, L. W. Martin, New modalities of strain-control of ferroelectric thin films, *Journal of Physics: Condensed Matter*, **28**, 263001 (2016).

[4] D. G. Schlom, L. Q. Chen, C. B. Eom, K. M. Rabe, S. K. Streiffer, J. M. Triscone, Strain tuning of ferroelectric thin films, *Annual Review of Materials Research*, **37**, 589 (2007).

[5] D. G. Schlom, L. Q. Chen, C. J. Fennie, V. Gopalan, D. A. Muller, X. Pan, R. Ramesh, R. Uecker, Elastic strain engineering of ferroic oxides, *MRS Bulletin*, **39**, 118 (2014).

[6] K. J. Choi, M. Biegalski, Y. Li, A. Sharan, J. Schubert, R. Uecker, P. Reiche, Y. Chen, X. Pan, V. Gopalan, L. Q. Chen, D. G. Schlom, and C. B. Eom, Enhancement of ferroelectricity in strained $BaTiO_3$ thin films, *Science*, **306**, 1005 (2004).

[7] J. Haeni, P. Irvin, W. Chang, R. Uecker, P. Reiche, Y. Li, S. Choudhury, W. Tian, M. Hawley, B. Craigo, A. K. Tagantsev, X. Q. Pan, S. K. Streiffer, L. Q. Chen, S. W. Kirchoefer, J. Levy and D. G. Schlom, Room-temperature ferroelectricity in strained $SrTiO_3$, *Nature*, **430**, 758 (2004).

[8] R. Zeches, M. Rossell, J. Zhang, A. Hatt, Q. He, C. H. Yang, A. Kumar, C. Wang, A. Melville, C. Adamo, G. Sheng, Y. H. Chu, J. F. Ihlefeld, R. Erni, C. Ederer, V. Gopalan, L. Q. Chen, D. G. Schlom, N. A. Spaldin, L. W. Martin, and R. Ramesh, A strain-driven morphotropic phase boundary in $BiFeO_3$, *Science*, **326**, 977 (2009).

[9] L. Zhang, J. Chen, L. Fan, O. Diéguez, J. Cao, Z. Pan, Y. Wang, J. Wang, M. Kim, S. Deng, J. Wang, H. Wang, J. Deng, R. Yu, J.s F. Scott, and X. Xing, Giant polarization in super-tetragonal thin films through interphase strain, *Science*, **361**, 494 (2018).

[10] L. Egerton, D. M. Dillon, Piezoelectric and dielectric properties of ceramics in the system potassium—sodium niobate, *Journal of the American Ceramic Society*, **42**, 438 (1959).

[11] Y. Saito, H. Takao, T. Tani, T. Nonoyama, K. Takatori, T. Homma, T. Nagaya, M. Nakamura, Lead-free piezoceramics, *Nature*, **432**, 84 (2004).

[12] H. Liu, H. Wu, K. P. Ong, T. Yang, P. Yang, P. K. Das, X. Chi, Y. Zhang, C. Diao, W. K. A. Wong, E. P. Chew , Y. Chen, C. K. I. Tan, A. Rusydi, M. B. H. Breese , D. J. Singh , L. Chen, S. J. Pennycook, and K. Yao, Giant piezoelectricity in oxide thin films with nanopillar structure, *Science*, **369**, 292 (2020).

[13] Y. Si, T. Zhang, C. Liu, S. Das, B. Xu, R. G. Burkovsky, X. K. Wei, Z. Chen, Antiferroelectric oxide thin-films: Fundamentals, properties, and applications, *Progress in Materials Science*, **142**, 101231 (2024).

[14] M. H. Zhang, L. Fulanović, C. Zhao, J. Koruza, Review on field-induced phase transitions in lead-free $NaNbO_3$-based antiferroelectric perovskite oxides for energy storage, *Journal of Materiomics*, **9**, 1(2023).

[15] B. Lin, K. P. Ong, T. Yang, Q. Zeng, H. K. Hui, Z. Ye, C. Sim, Z. Yen, P. Yang, Y. Dou, X. Li, X. Gao, C. K. I. Tan, Z. S. Lim, S. Zeng, T. Luo, J. Xu, X. Tong, P. W. F. Li, M. Ren, K. Zeng, C. Sun, S. Ramakrishna, M. B. H. Breese, C. Boothroyd, C. Lee, D. J. Singh, Y. M. Lam and H. Liu, Ultrahigh electromechanical response from competing ferroic orders, *Nature*, **633**, 798 (2024).

[16] A. Kania, J. Kwapulinski, $Ag_{1-x}Na_xNbO_3$ (ANN) solid solutions: from disordered antiferroelectric $AgNbO_3$ to normal antiferroelectric $NaNbO_3$, *Journal of Physics: Condensed Matter*, **11**, 8933 (1999).

[17] H. D. Megaw, The seven phases of sodium niobate, *Ferroelectrics*, **7**, 87 (1974).

[18] C. A. Randall, Z. Fan, I. Reaney, L.Q. Chen, S. Trolier-McKinstry, Antiferroelectrics: History, fundamentals, crystal chemistry, crystal structures, size effects, and applications, *Journal of the American Ceramic Society*, **104**, 3775 (2021).

[19] Z. Liu, T. Lu, J. Ye, G. Wang, X. Dong, R. Withers, Y. Liu, Antiferroelectrics for energy storage applications: a review, *Advanced Materials Technologies*, **3**, 1800111 (2018).

[20] H. Yang, C. Bin, Y. Zhao, X. Hou, J. Zhang, L. Liao, H. Zhou, Y. Liu, J. Wang, A novel low-loss and high-stability (1-x)$Na_{0.98}NbO_{3-x}Bi$ $(Al_{0.5}Y_{0.5})O_3$ lead-free composite ceramics for dielectric energy storage capacitors, *Chemical Engineering Journal*, **475**, 146426 (2023).

[21] Y. Zhen, J. F. Li, Normal sintering of (K, Na) NbO_3-based ceramics: influence of sintering temperature on densification, microstructure, and electrical properties, *Journal of the American Ceramic Society*, **89**, 3669 (2006).

[22] J. Schwarzkopf, M. Schmidbauer, T. Remmele, A. Duk, A. Kwasniewski, S. Bin Anooz, A. Devi, R. Fornari, Strain-induced phase transitions in epitaxial $NaNbO_3$ thin films grown by metal–organic chemical vapour deposition, *Journal of Applied Crystallography*, **45**, 1015 (2012).

[23] S. Bin Anooz, Y. Wang, P. Petrik, M. de Oliveira Guimaraes, M. Schmidbauer, J. Schwarzkopf, High temperature phase transitions in $NaNbO_3$ epitaxial films grown under tensile lattice strain, *Applied Physics Letters*, **120**, 202901 (2022).

[24] R. Wördenweber, J. Schwarzkopf, E. Hollmann, A. Duk, B. Cai, M. Schmidbauer, Impact of compressive in-plane strain on the ferroelectric properties of epitaxial $NaNbO_3$ films on (110) $NdGaO_3$, *Applied Physics Letters*, 103, 132908 (2013).

[25] T. Schneider, J. Cardoletti, P. Komissinskiy, L. Alff, Impact of Strain Engineering on Antiferroelectricity in $NaNbO_3$ Thin Films, *ACS Omega*, 2023, 8, 23587 (2023).

[26] T. Schneider, J. Cardoletti, H. Ding, M. H. Zhang, T. Jiang, M. Major, P. Komissinskiy, L. Molina-Luna, L. Alff, Evidence for antipolar displacements in $NaNbO_3$ thin films, *Applied Physics Letters*, **121**, 122906 (2022).

[27] R. Xu, K.J. Crust, V. Harbola, R. Arras, K.Y. Patel, S. Prosandeev, H. Cao, Y.T. Shao, P. Behera, L. Caretta, W. J. Kim, A. Khandelwal, M. Acharya, M. M. Wang, Y. Liu, E. S. Barnard, A. Raja, L. W. Martin, X. W. Gu, H. Zhou, R. Ramesh, D. A. Muller, L. Bellaiche, H. Y. Hwang, Size-Induced Ferroelectricity in Antiferroelectric Oxide Membranes, *Advanced Materials*, **35**, 2210562 (2023).

[28] J. P. Perdew, A. Ruzsinszky, G. I. Csonka, O. A. Vydrov, G. E. Scuseria, L. A. Constantin, X. Zhou, K. Burke, Restoring the density-gradient expansion for exchange in solids and surfaces, *Physical review Letters*, **100**, 136406 (2008).

[29] P. Blaha, Karlheinz Schwarz, Georg K H Madsen, Dieter Kvasnicka, Joachim Luitz, Robert Laskowsk, Fabien Tran, Laurence Marks, L. Marks, WIEN2k: An Augmented Plane Wave Plus Local Orbitals Program for Calculating Crystal Properties., *Techn. Universitat*, 2021.

[30] A. Sakowski-Cowley, K. Łukaszewicz, H. D. Megaw, The structure of sodium niobate at room temperature, and the problem of reliability in pseudosymmetric structures, *Acta Crystallographica Section B: Structural Crystallography and Crystal Chemistry*, **25**, 851 (1969).

[31] A. Vailionis, H. Boschker, W. Siemons, E.P. Houwman, D. H. Blank, G. Rijnders, G. Koster, Misfit strain accommodation in epitaxial ABO_3 perovskites: Lattice rotations and lattice modulations, *Physical Review B*, **83**, 064101 (2011).

[32] A. Biswas, C. H. Yang, R. Ramesh, Y. H. Jeong, Atomically flat single terminated oxide substrate surfaces, *Progress in Surface Science*, **92**, 117 (2017).

[33] C. Adamo, X. Ke, H. Wang, H. Xin, T. Heeg, M. Hawley, W. Zander, J. Schubert, P. Schiffer, D. Muller, L. Maritato and D. G. Schlom, Effect of biaxial strain on the electrical and

magnetic properties of (001) $La_{0.7}Sr_{0.3}MnO_3$ thin films, *Applied Physics Letters*, **95**, 112504 (2009).

[34] D. Han, M. Bouras, C. Botella, A. Benamrouche, B. Canut, G. Grenet, G. Saint-Girons, R. Bachelet, Poisson ratio and bulk lattice constant of $(Sr_{0.25}La_{0.75})CrO_3$ from strained epitaxial thin films, *Journal of Applied Physics*, **126**, 085304 (2019).

[35] J. Sellmann, J. Schwarzkopf, A. Kwasniewski, M. Schmidbauer, D. Braun, A. Duk, Strained ferroelectric $NaNbO_3$ thin films: Impact of pulsed laser deposition growth conditions on structural properties, *Thin Solid Films*, **570**, 107 (2014).

[36] M. L. Dunn, H. Ledbetter, Poisson's ratio of porous and microcracked solids: Theory and application to oxide superconductors, *Journal of Materials Research*, **10**, 2715 (1995).

[37] H. Ledbetter, M. Lei, S. Kim, Elastic constants, debye temperatures, and electron-phonon parameters of superconducting cuprates and related oxides, *Phase Transitions: A Multinational Journal*, 23, 61 (1990).

[38] Q. Zeng, C. Sim, A. M. Yong, H. K. Hui, Y. Chen, L. Zhang, C. K. I. Tan, H. Liu, K. Zeng, Emerging multi-frequency surface strain force microscopy, *Journal of Applied Physics*, **133**, 040901 (2023).

[39] G. Rijnders, D. H. Blank, Growth kinetics during pulsed laser deposition, *Pulsed Laser Deposition of Thin Films*, John Wiley & Sons, Inc., New Jersey, USA 2007.

[40] S. Tian, C. Wang, Y. Zhou, X. Li, P. Gao, J. Wang, Y. Feng, X. Yao, C. Ge, M. He, M. He, X. Bai, G. Yang and K. Jin, Manipulating the ferroelectric domain states and structural distortion in epitaxial $BiFeO_3$ ultrathin films via Bi nonstoichiometry, *ACS Applied Materials & Interfaces*, **10**, 43792 (2018).

[41] Z. Xi, J. Ruan, C. Li, C. Zheng, Z. Wen, J. Dai, A. Li, D. Wu, Giant tunnelling electroresistance in metal/ferroelectric/semiconductor tunnel junctions by engineering the Schottky barrier, *Nature communications*, **8**, 15217 (2017).

[42] M. Schmidbauer, J. Sellmann, D. Braun, A. Kwasniewski, A. Duk, J. Schwarzkopf, Ferroelectric domain structure of $NaNbO_3$ epitaxial thin films grown on (110) $DyScO_3$ substrates, *Physica Status Solidi (RRL)–Rapid Research Letters*, 8, 522 (2014).

[43] J. M. Rondinelli, S. J. May, J. W. Freeland, Control of octahedral connectivity in perovskite oxide heterostructures: An emerging route to multifunctional materials discovery, *MRS Bulletin*, **37**, 261 (2012).

[44] G. Sheng, J. X. Zhang, Y. L. Li, S. Choudhury, Q. X. Jia, Z. K. Liu and L. Q. Chen, Domain stability of PbTiO3 thin films under anisotropic misfit strains: Phase-field simulations, *Journal of Applied Physics*, **104**, 054105 (2008).

[45] G. Catalan, J. Seidel, R. Ramesh, J. F. Scott, Domain wall nanoelectronics, *Reviews of Modern Physics*, **84**, 119 (2012).

[46] D. Meier, S. M. Selbach, Ferroelectric domain walls for nanotechnology, *Nature Reviews Materials*, **7**, 157 (2022).

[47] J. J. Wang, B. Wang, L. Q. Chen, Understanding, predicting, and designing ferroelectric domain structures and switching guided by the phase-field method, *Annual Review of Materials Research*, **49**, 127 (2019).

[48] A. V. Kimmel, P. M. Weaver, M. G. Cain, P. V. Sushko, Defect-mediated lattice relaxation and domain stability in ferroelectric oxides, *Physical Review Letters*, **109**, 117601 (2012).

FIGURES AND CAPTION

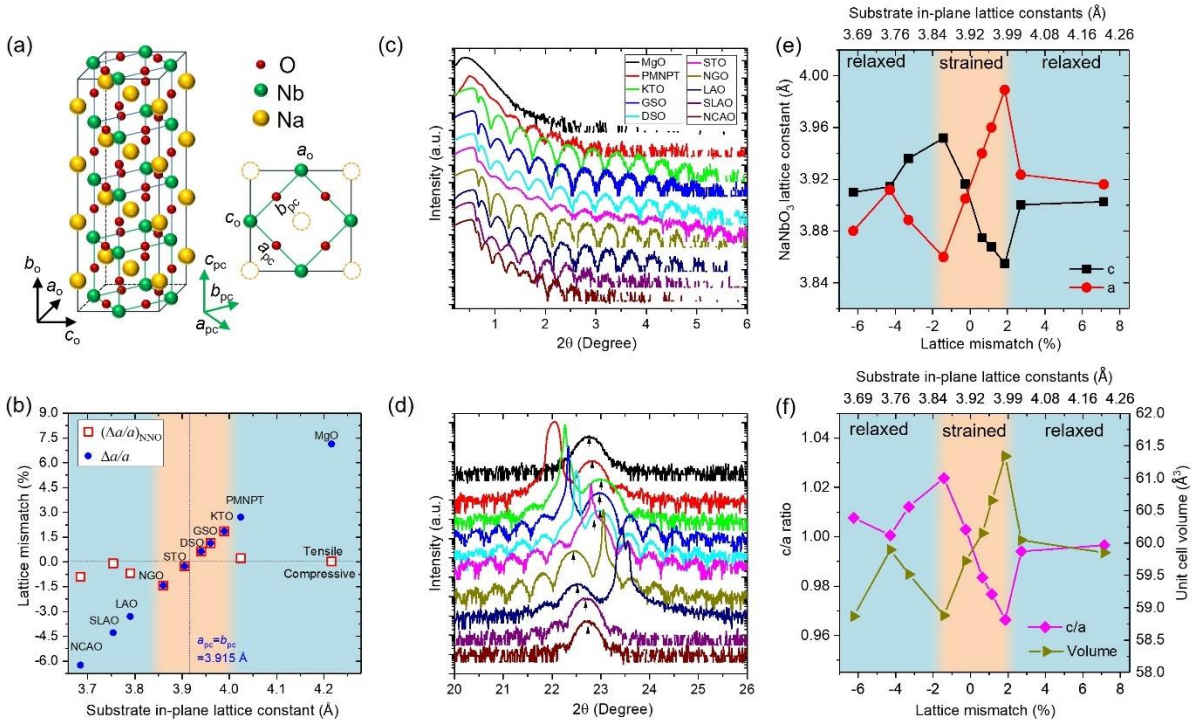

Figure 1. Crystal structure, lattice mismatch and X-ray diffraction data of NNO thin films on ten different substrates. (a) Schematic structure of NNO in orthorhombic structure of bulk NNO, a_o, b_o, c_o are the axes of orthorhombic structure. The green lines indicate the pseudocubic unit cell, a_{pc}, b_{pc}, c_{pc} are the axes of pseudocubic structure (left panel). The relationship between orthorhombic and pseudocubic unit cell for a_{pc}-b_{pc} plane of NNO (right panel). The dashed yellow circles represent the Na atoms, which are positioned in a different plane from the Nb-O plane. (b) The in-plane lattice mismatch between NNO bulk and various substrates $\Delta a/a$, and the in-plane lattice mismatch between NNO bulk and the deposited NNO thin films $(\Delta a/a)_{NNO}$. The mismatch $\Delta a/a$ is calculated using the formula $\Delta a/a = (a_s - a_b)/a_s$, where a_s is the lattice parameter of the substrate and a_b is the lattice parameter NNO bulk, respectively. The mismatch $(\Delta a/a)_{NNO}$ is calculated using the formula $(\Delta a/a)_{NNO} = (a_f - a_b)/a_f$, where a_f is the in-plane lattice parameter of the deposited NNO thin films. The pseudocubic lattice parameters of NNO bulk are used in this plot. The lattice mismatch is calculated assuming that NNO on the substrates

are oriented along $(001)_{pc}$ direction. (c) Low-angle X-ray reflectivity (XRR) of NNO thin films on various substrates. Clear oscillations indicate high quality and smooth surface of the NNO thin films. (d) X-ray diffraction (XRD) patterns of NNO thin films on different substrates in the 2θ angles between 20-26°. The thickness fringes indicate high quality of the NNO thin films. The black arrows serve as visual guides to indicate the changes in the NNO $(001)_{pc}$ diffraction peak positions. For clarity, the XRR and XRD curves are shifted in the vertical direction. (e) The out-of-plane lattice constant *c* and in-plane lattice constant *a* of NNO thin films as a function of the in-plane lattice mismatch between NNO and substrates (bottom *x*-axis), and in-plane lattice constants of different substrates (top *x*-axis). (f) The *c/a* ratio and unit cell volume of NNO thin films.

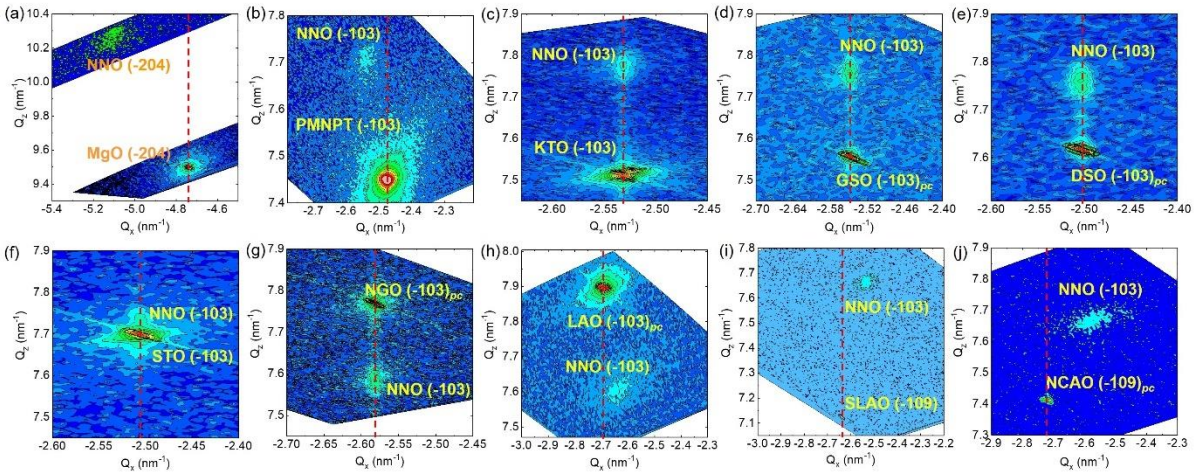

Figure 2. Reciprocal space maps (RSMs) of NNO thin films deposited on single crystal substrates of (a) MgO, (b) PMNPT, (c) KTO, (d) GSO, (e) DSO, (f) STO, (g) NGO, (h) LAO, (i) SLAO, and (j) NCAO. For MgO substrate, the measurement region is in the vicinity of the asymmetric -204 Bragg reflection of the substrate. For SLAO and NCAO substrates, the measurement region is in the vicinity of the asymmetric -109 Bragg reflection. For rest substrates, the measurement region is in the vicinity of the asymmetric -103 Bragg reflection. The labels $(-103)_{pc}$ for GSO, DSO, NGO, LAO substrates indicate the -103 reflection in pseudocubic notation. The red dash lines serve as visual guides to indicate the horizontal shift of NNO diffraction spots compared to those of the substrates.

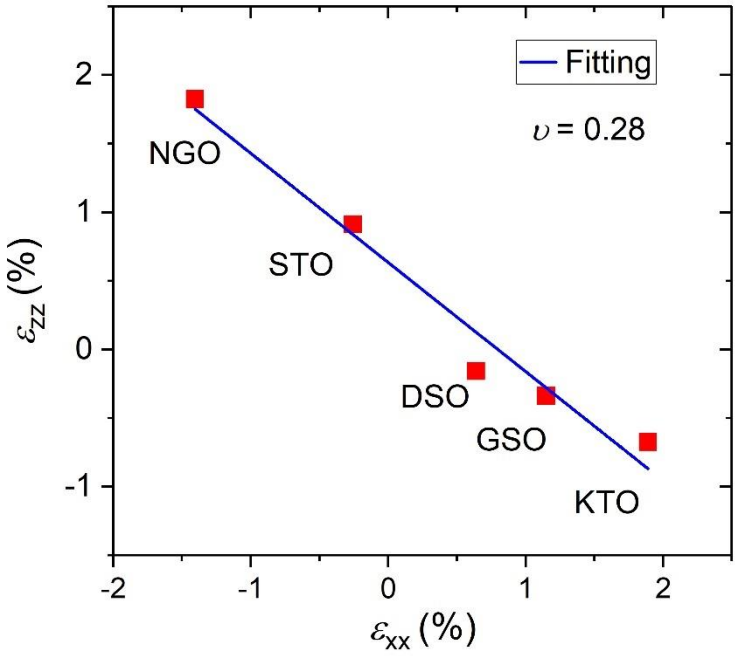

Figure 3. The out-of-plane lattice strain ε_{zz} *versus* the in-plane lattice strain ε_{xx} of $NaNbO_3$ thin films on NGO, STO, DSO, GSO and KTO substrates, within the fully strained region. The out-of-plane lattice strain is calculated using the formula $\varepsilon_{zz} = (c_f - c_{bulk})/c_{bulk}$, where c_f and c_{bulk} represent the out-of-plane lattice parameters of the NNO thin film and bulk material, respectively. The in-plane lattice strain is calculated using the formula $\varepsilon_{xx} = (a_f - a_{bulk})/c_{bulk}$, where a_f and a_{bulk} represent the out-of-plane lattice parameters of the NNO thin film and bulk material, respectively. The c_f and a_f of NNO thin films are obtained from the measured values as shown in **Figure 1(e)**. The c_{bulk} and a_{bulk} of bulk NNO are obtained based on pseudocubic notation: a_{bulk} = 3.915 Å, c_{bulk} = 3.881 Å. The Poisson's ratio v of NNO can be calculated from the formula $v=1/(1-2\varepsilon_{xx}/\varepsilon_{zz})$, which give v = 0.28. The $\varepsilon_{zz}/\varepsilon_{xx}$ value of -0.7953 is estimated by a linear fit (blue line) to the ε_{zz} *versus* ε_{xx} data.

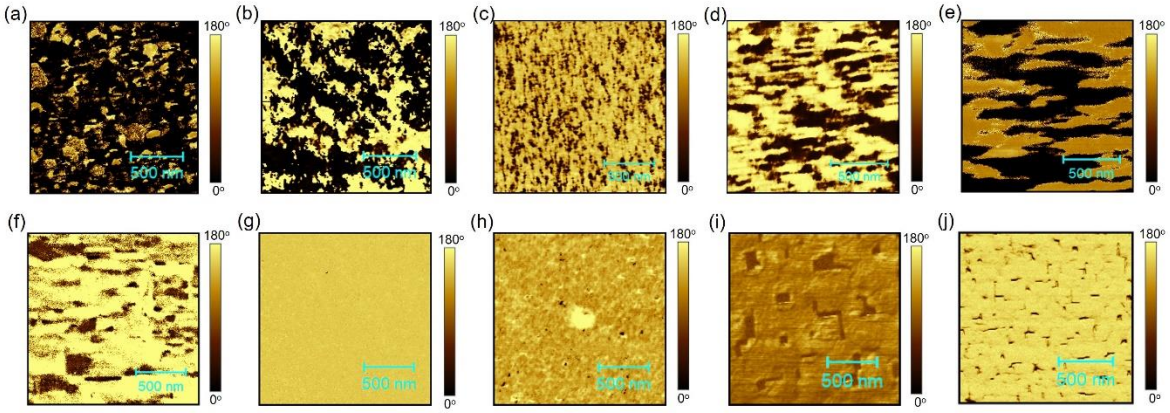

Figure 4. The vertical PFM phase images of NNO thin films deposited on different substrates of (a) MgO, (b) PMNPT, (c) KTO, (d) GSO, (e) DSO, (f) STO, (g) NGO, (h) LAO, (i) SLAO, and (j) NCAO.

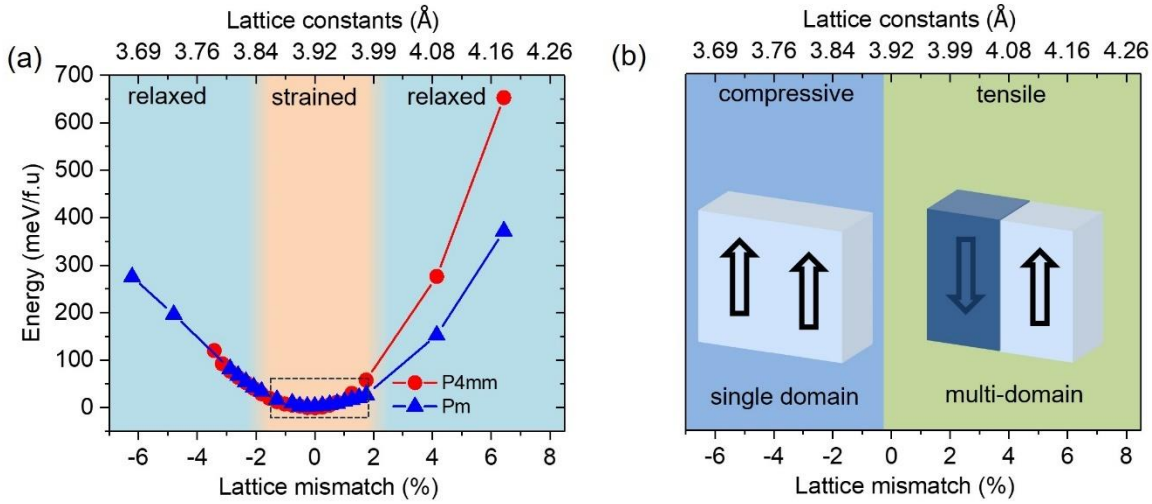

Figure 5. (a) The calculated energy for crystal structures with space group of *Pm* and *P4mm* as a function of the in-plane lattice mismatch between NNO and substrates (bottom *x*-axis), and in-plane lattice constants of different substrates (top *x*-axis). f.u. means formula unit. The dashed black rectangle indicates the energy range for the strained films. (b) The schematic ferroelectric domain structures for NNO thin films with different strain states. The arrows indicate the vertical direction of polarization.

Abstract Graphic